CMS Physics Analysis Summary

Contact: cms-pag-conveners-smp@cern.ch 2021/03/24

A precision measurement of the W boson decay branching fractions in pp collisions at $\sqrt{s} = 13$ TeV

The CMS Collaboration

Abstract

The leptonic and inclusive hadronic decay branching fractions of the W boson are studied using 35.9 fb^{-1} of proton-proton collision data collected at $\sqrt{s} = 13$ TeV during the 2016 run of the CMS experiment. Events characterized by the production of two W boson, or of a W boson accompanied by jets, are selected. Multiple event categories sensitive to the signal processes are defined based on the presence of energetic isolated charged leptons, the number of hadronic jets, and the number of b-tagged jets. A maximum likelihood estimate of the W branching fractions is carried out by fitting to the data in each event category simultaneously. The branching fractions of the W boson decaying into electron, muon, and tau lepton final states amount to $(10.83 \pm 0.1)\%$, $(10.94 \pm 0.08)\%$, and $(10.77 \pm 0.21)\%$, respectively, supporting the hypothesis of lepton universality for the weak interaction. Under the assumption of lepton universality, the inclusive leptonic and hadronic decay branching fractions are found to be $(10.89 \pm 0.08)\%$ and $(67.32 \pm 0.23)\%$, respectively. From these results, three standard model quantities are subsequently derived: the sum square of elements in the first two rows of the Cabibbo-Kobayashi-Maskawa (CKM) matrix $\sum |V_{ij}|^2 = 1.989 \pm 0.021$, the CKM element $|V_{cs}| = 0.969 \pm 0.011$, and the strong coupling constant at the W mass scale, $\alpha_S(m_W) = 0.094 \pm 0.033$.

1 Introduction

The study of the W boson leptonic and hadronic widths $\Gamma(\mathrm{W} \to \ell\overline{\nu}, \mathrm{h})$ or, similarly, of their corresponding decay branching fractions $\mathcal{B}(\mathrm{W} \to \ell\overline{\nu}, \mathrm{h}) = \Gamma(\mathrm{W} \to \ell\overline{\nu}, \mathrm{h})/\Gamma_{\mathrm{W,tot}}$, provides a useful testing ground for various fundamental aspects of the standard model (SM) of particle physics. Primarily, the SM electroweak bosons are assumed to couple equally to all three lepton generations, a property known as lepton universality (LU). Experimental evidence of a departure from this assumption would be a sign of new physics contributing to SM decays. In the recent years, hints of potential LU violation have been observed in rare semileptonic decays of B mesons, although their interpretation is hindered by quantum chromodynamics (QCD) uncertainties [1, 2]. A complementary, and potentially "cleaner", test of lepton universality can be carried out by comparing the three leptonic branching fractions of the W boson in the electron, muon, and tau decay channels. The most precise determinations of the $\mathcal{B}(\mathrm{W} \to \ell\overline{\nu})$ fractions have been obtained from combinations of measurements carried out by each of the four LEP experiments [3]. Based on those, a ratio between the τ and the average of lighter lepton branching fractions, to test the LU hypothesis, has been derived

$$R_{\tau/\ell} = \frac{2\,\mathcal{B}(\mathrm{W} \to \tau\overline{\nu}_\tau)}{\mathcal{B}(\mathrm{W} \to \mathrm{e}\overline{\nu}_\mathrm{e}) + \mathcal{B}(\mathrm{W} \to \mu\overline{\nu}_\mu)} = 1.066 \pm 0.025\,, \tag{1}$$

which shows a 2.6 standard deviation with respect to the SM prediction of $R_{\tau/\ell} = 0.9991$ [4–6]. Confirmation or refutation of such a possible LU violation requires more precise measurements of the W branching fractions than so-far available. In pp collisions at the LHC, the large cross section for the production of top quark pairs, which each correspondingly decay into a W boson and a bottom b quark, offers a sizable and high-purity W boson data sample for the study of its various decay channels. A recent measurement by the ATLAS collaboration has exploited such a strategy to measure the $R_{\tau/\mu}$ ratio by fitting the impact parameter distribution of the final state decay muons [7]. The resulting value of $R_{\tau/\mu} = 0.992 \pm 0.013$ is in tension with the LEP result, Eq. (1), and supports the LU hypothesis.

In addition, within the SM, the hadronic width of the W boson depends on various free parameters of the theory, such as the strong coupling constant α_S, and the quark flavor mixing elements of the first two rows of the Cabibbo–Kobayashi–Maskawa (CKM) matrix. Theoretically, the decay width of the W boson into (massless) quarks can be determined via the following expression:

$$\Gamma(\mathrm{W} \to \mathrm{h}) = \frac{\sqrt{2}\mathrm{G_F}\,\mathrm{N_c}}{12\pi} m_\mathrm{W}^3 \sum_{\mathrm{i,j}} |\mathrm{V_{ij}}|^2 \left(1 + \sum_{i=1}^{4} c_\mathrm{QCD}^{(i)} \left(\frac{\alpha_\mathrm{S}}{\pi}\right)^i + \delta_\mathrm{EW}(\alpha) + \delta_\mathrm{mix}(\alpha\alpha_\mathrm{S})\right), \tag{2}$$

where the prefactor in front of the parentheses is the Born W boson width that depends on the number of colors $\mathrm{N_c} = 3$, the Fermi constant $\mathrm{G_F}$, the W boson mass m_W, and the squared sum of CKM matrix elements $|\mathrm{V_{ij}}|$ (summed over ij = ud, us, ub, cd, cs, cb quark pairs, because the top-quark is not kinematically accessible). The rest of terms in Eq. (2) include the higher-order perturbative QCD corrections, given by an expansion in α_S^i coefficients known up to order $i = 4$ [8], the electroweak corrections δ_ew known to order $\mathcal{O}(\alpha)$ [4], and the mixed electroweak plus QCD corrections δ_mix known to order $\mathcal{O}(\alpha\alpha_\mathrm{S})$ [9]. Based on Eq. (2), from the ratio of the hadronic to leptonic branching fractions of the W boson, one can thereby precisely test the unitarity of the two first CKM matrix rows, i.e. search for any significant deviation with respect to $\sum_{\mathrm{u,c,d,s,b}} |\mathrm{V_{ij}}|^2 \equiv 2$, and, in particular, indirectly determine the least precisely known CKM element $|\mathrm{V_{cs}}|$ [3, 10]. From the experimental CKM element values today [11], one obtains $\sum_{\mathrm{u,c,d,s,b}} |\mathrm{V_{ij}}|^2 = 2.0235 \pm 0.0225$, with a 1.1% uncertainty dominated by that of the $|\mathrm{V_{cs}}|$ measurement. Therefore, any determination of the W inclusive hadronic branching fraction with

subpercent uncertainties provides a more precise, albeit indirect, determination of this sum and/or of the $|V_{cs}|$ value.

This note describes a precision measurement of the three leptonic W boson branching fractions, as well as of the inclusive hadronic one assuming lepton universality, and their use to test LU and constrain various SM parameters. The analysis is based on a data sample of proton-proton collisions at a center-of-mass energy of 13 TeV corresponding to an integrated luminosity of 35.9 fb^{-1} recorded by the CMS experiment during the 2016 run. Events are collected online using single charged lepton triggers that require at least one prompt electron or muon with large transverse momentum. The offline analysis defines categories of final states consistent with the production of two W bosons, or a W boson plus jets, that decay leptonically. Estimation of the values of the W branching fractions is then carried out through a binned maximum likelihood fit of multiple event categories, where the selected final states are classified according to the number of jets and the number of those jets identified as originating from bottom quarks, and further binned by channel-dependent kinematic information.

2 The CMS detector

The central feature of the CMS apparatus is a superconducting solenoid, 13 m in length and 6 m in diameter, which provides an axial magnetic field of 3.8 T. Within the field volume there are several particle detection systems. Charged particle trajectories are measured by silicon pixel and strip trackers, covering $0 \leq \phi \leq 2\pi$ in azimuth and $|\eta| < 2.5$ in pseudorapidity, where η is defined as $-\log[\tan(\theta/2)]$ and θ is the polar angle of the trajectory of the particle with respect to the counterclockwise proton beam direction. A lead-tungstate crystal electromagnetic calorimeter (ECAL) and a brass/scintillator hadron calorimeter (HCAL) surround the tracking volume and cover the region $|\eta| < 3$. The calorimeters provide energy measurements of photons, electrons, and jets of hadrons. A lead/silicon-strip preshower detector is located in front of the ECAL endcap. Muons are identified and measured in gas-ionization detectors embedded in the steel return yoke outside of the solenoid. The detector is nearly hermetic, allowing energy balance measurements in the plane transverse to the beam direction. A more detailed description of the CMS detector can be found in Ref. [12].

3 Simulated data samples

Simulated Monte Carlo (MC) data samples are generated for modelling the signal ($t\bar{t}$, tW, WW, and W+jets) and background (Z+jets, WZ and ZZ) processes. The contribution to the background originating from multijet QCD production is estimated using data-driven methods.

The POWHEG v2 [13–17] MC event generator is used to produce samples of $t\bar{t}$, single top (tW), and most of the diboson processes (WW, WZ, ZZ $\to 2\ell 2\nu$). The W+jets samples are generated at leading order (LO) in QCD using the MADGRAPH code [18]. Drell–Yan, WZ, and the non-fully leptonic ZZ decay modes, are generated at next-to-leading-order (NLO) QCD accuracy with MADGRAPH_aMC@NLO v.2.2.2 [19, 20]. In all cases, the MC samples are generated with the NNPDF3.0 parton distribution functions (PDFs), and are interfaced with PYTHIA 8.2 for parton shower and hadronization using the underlying event (UE) tune CUETP8M2T4 [21, 22]. The CMS detector response is simulated with a GEANT4-based model [23], and the events are reconstructed and analyzed using the same software employed to process collision data.

The impact of pileup pp collisions on the event reconstruction is taken care of in the simulation by superimposing simulated minimum bias events on top of each process of interest. Because

the distribution of the number of pileup events in the original simulation is not the same as in data, the former is reweighted to match the latter. Correction factors are also applied to account for differences between data and simulation with respect to modelling of the trigger efficiencies, as well as lepton reconstruction, identification, and isolation efficiencies. Additional corrections are applied to account for the energy scale and lepton p_T resolution. The observed jet energy scale and resolution, top quark p_T distribution, and b tagging efficiency and multivariate discriminator distributions in data, are used to correct the simulated events. Lepton universality is assumed by default in the simulated data sets, taking $\mathcal{B}(W \to \ell\overline{\nu}) = 10.8\%$ for each leptonic decay mode. The hadronic and leptonic branching fractions of the tau lepton are taken from their current world average values [11].

4 Event selection and reconstruction

The measurement is based on a data sample corresponding to an integrated luminosity of $35.9\,\text{fb}^{-1}$ of proton-proton collisions at a center-of-mass energy of 13 TeV collected by the CMS experiment at the LHC during 2016. A two-tier trigger system [24] selects pp collision events of interest for physics analysis. The triggers used here require the production of a single muon or electron with transverse momentum, p_T, greater than 24 GeV and 27 GeV, respectively.

The physics processes of interest for this study include $t\bar{t}$, tW, WW, and W+jets production. The background processes comprise the multiple production of QCD jets, Z boson plus jets, and WZ and ZZ diboson production. Selecting a data sample of events with a final state consistent with the signal processes defined above requires reconstructing electrons, muons, hadronically decaying tau leptons, and hadronic jets. Additionally, in order to suppress backgrounds it is useful to determine whether the reconstructed jets have originated from light quarks or gluons, or from the fragmentation of b quarks.

The global event reconstruction, also called particle-flow (PF) event reconstruction [25], aims at reconstructing and identifying each individual particle in a pp collision, with an optimized combination of all subdetector information. In this process, the identification of the particle type (photon, electron, muon, charged hadron, neutral hadron) plays an important role in the determination of the particle direction and energy. Photons are identified as ECAL energy clusters not linked to the extrapolation from any charged particle trajectory reconstructed in the tracker. Electrons are identified as a primary charged particle track plus, potentially, any energy clusters corresponding to this track extrapolated to the ECAL, as well as to any bremsstrahlung photons emitted along the way through the tracker material. Muons are identified as tracks in the central tracker consistent with either a track or several hits in the muon system, and associated with calorimeter deposits compatible with the muon hypothesis. Charged hadrons are identified as charged particle tracks neither identified as electrons, nor as muons. Finally, neutral hadrons are identified as HCAL energy clusters not linked to any charged hadron trajectory, or as ECAL and HCAL signals with energies above those expected to be deposited by a charged hadron.

Primary pp collision vertices (PVs) are reconstructed using information from the tracking subsystem, mainly the inner pixel detector. Quality cuts are applied to reconstructed PVs to guarantee that they come from a hard scattering event. The requirements for identifying good primary vertices are $N_{\text{d.o.f.}} > 4$, $|z| < 24$ cm, and $\sqrt{x^2 + y^2} < 2$ cm [26]. The PVs are ordered based on the sum p_T of the tracks used in their reconstruction, and the selected physics objects are associated to the PV with the greatest sum p_T.

Muon candidates are reconstructed using both the muon and tracker detector subsystems. The

coverage of these two detector systems allows reconstructing muons within $|\eta| < 2.4$ and with p_T as low as 5 GeV [27]. Muons are required to be reconstructed by both the global and tracker reconstruction algorithms. These algorithms are distinct in that the latter $\mu^{\pm}$ reconstruction begins with tracker information and extrapolates the trajectory to find consistency with hits in the muon system, whereas the global muon algorithm inverts the reconstruction steps starting from the muon system and finding trajectories in the tracker that are consistent with them. The combination of these two algorithms results in a muon reconstruction that is efficient in detecting muons within the detector acceptance as well as accurate in predicting their momenta.

For the purpose of selecting muons specifically coming from W boson decays, a set of additional identification and isolation requirements are applied [28]. The muon identification requirements are designed to have high selection efficiency and a low probability of misidentification against nonprompt muons. The isolation of muons is calculated via a variable *Iso* defined as the p_T sum of all charged hadron, neutral hadron, and photon PF candidates in a cone of radius $\Delta R = \sqrt{\Delta\eta^2 + \Delta\phi^2} = 0.4$ around the μ candidate direction. This variable includes also a contribution to remove the contamination from neutral particles produced in other overlapping pp collisions by subtracting (half) the average energy deposited by pileup as,

$$Iso_{\mathrm{PF}} = Iso_{\mathrm{ch.had}} + \max\left(0, Iso_{\mathrm{neu.had}} + Iso_{\gamma} - 0.5 Iso_{\mathrm{pileup}}\right) . \quad (3)$$

Electrons are reconstructed by combining information from the ECAL and the tracking system using a Gaussian-sum filter method [29]. Electrons are required to have $p_T > 10$ GeV, and lie within the geometrical acceptance of $|\eta| < 2.5$ [30]. Corrections are applied to account for mismeasurements of the electron momentum scale and resolution. Electrons are required to pass tight isolation criteria. The isolation variable is constructed by summing the energy of charged and neutral PF objects within a cone of radius $\Delta R = 0.4$ around the electron candidate direction, and subtracting off the contribution from pileup. The combined PF isolation with pileup correction variable for $e^{\pm}$ candidates is defined as

$$Iso_{\mathrm{comb}} = Iso_{\mathrm{ch.had.}} + \max\left(0, Iso_{\mathrm{neu.had.}} + Iso_{\gamma} - \rho A_{\mathrm{eff}}(|\eta_e|)\right) , \quad (4)$$

and depends on the parameter ρ, which correlates with the average energy density in the event due to pileup, and on the effective detector area A_{eff}, which changes depending on the $|\eta|$ of the electron [31, 32].

Hadronically decaying τ leptons are reconstructed using the hadron-plus-strips algorithm [33]. This algorithm reconstructs tau candidates seeded by a PF jet that is consistent with either a single or a triple charged pion decay of the τ lepton. In the single charged pion decay mode, neutral pions are detected by reconstructing their diphoton decays. Tau events that include the production of additional muons or electrons are rejected by an overlap veto. Jets not originating from τ decays are rejected by a multivariate discriminator that takes into account the pileup contribution to the neutral component of the τ decay [33]. The reconstructed hadronic tau leptons are required to have $p_T > 20$ GeV and $|\eta| < 2.3$. A working point with an identification efficiency of ≈50% and a misidentification efficiency of ≈0.2% is used in selecting reconstructed hadronic tau decays. The scale factors accounting for differences of tau identification efficiencies in the simulations with respect to the data, are determined in two control regions [33] enriched in $Z \to \tau\tau$ and $t\bar{t}$ production, respectively. The differences of the reconstructed tau energy between data and simulation are corrected for by scale factors determined from the $Z \to \tau\tau$ region.

Jets are reconstructed from PF candidates [25] clustered using the anti-k_T algorithm [34] with a distance parameter of $\Delta R = 0.4$, and are required to have $p_T > 30$ GeV and $|\eta| < 2.4$. Jets

Table 1: Baseline categorization of events based on the triggering electron or muon, the presence (or vetoing) of isolated reconstructed charged leptons, plus additional jets, identified or not as originating from a b quark. Kinematic criteria required on the charged leptons and jets are listed in the last column. Categories without hadrons in the final state require also the selected leptons to have opposite-sign charge.

trigger	label	N_e	N_μ	N_τ	N_j	N_b	additional requirements
e	ee	2	0	0	≥ 2	≥ 1	$p_T^e > 30, 20\,\text{GeV}$, $\lvert m_{ee} - m_Z \rvert > 15\,\text{GeV}$
	eμ	1	1	0	≥ 0	≥ 0	$p_T^e > 30\,\text{GeV}$, $p_T^\mu > 10\,\text{GeV}$
	eτ	1	0	1	≥ 0	≥ 0	$p_T^e > 30\,\text{GeV}$, $p_T^\tau > 20\,\text{GeV}$
	eh	1	0	0	≥ 4	≥ 1	$p_T^e > 30\,\text{GeV}$, $p_T^j > 30\,\text{GeV}$
μ	μe	1	1	0	≥ 0	≥ 0	$p_T^\mu > 25\,\text{GeV}$, $p_T^e > 20\,\text{GeV}$
	$\mu\mu$	0	2	0	≥ 2	≥ 1	$p_T^\mu > 25, 10\,\text{GeV}$, $\lvert m_{\mu\mu} - m_Z \rvert > 15\,\text{GeV}$
	$\mu\tau$	0	1	1	≥ 0	≥ 0	$p_T^\mu > 25\,\text{GeV}$, $p_T^\tau > 20\,\text{GeV}$
	μh	0	1	0	≥ 4	≥ 1	$p_T^\mu > 25\,\text{GeV}$, $p_T^j > 30\,\text{GeV}$

are corrected to account for pileup contamination, differences in absolute response of jet p_T between data and simulation, and relative response in η [35]. To reduce contamination from photons and prompt leptons, additional identification requirements are applied to the jets. Jets are vetoed if they overlap with any muons, electrons, or tau leptons passing the identification requirements described above, within a cone of radius $\Delta R = 0.4$.

The identification of jets originating from the decay of bottom (b) quarks is done using the cMVA b tagging algorithm [36] that optimizes the efficiency for identifying b jets while reducing the misidentification of jets originating from light quarks and gluons. To account for the difference in b tagging efficiency in data and simulation, the b tag status of each jet is modified based on a set of scale factors that depend on whether the jet originated from a b quark, c quark, or some other source. Such scale factors are determined as a function of the jet p_T [36].

5 Event categorization

The event selection begins by collecting data triggered by either a single isolated muon with $p_T > 24$ GeV or a single electron with $p_T \geq 27$ GeV. Offline, a number of additional requirements are then applied to categorize the events based on the multiplicity of reconstructed leptons, jets, and b-tagged jets, passing a given minimum p_T threshold each, as summarized in Table 1. In categories with two leptons in the final state, the leptons are required to have opposite-sign electric charge. Events in the ee and $\mu\mu$ categories are rejected if the lepton pair invariant mass is between 75 and 105 GeV in order to reduce the contamination from Drell–Yan events. The different categories are primarily dominated by signal events originating from $t\bar{t}$ production with minor contributions from tW, WW, or W+jets processes, and the background consists mainly of Drell–Yan and multijet QCD production, with almost negligible contributions from non-WW diboson processes.

Each of these selections is designed to target a particular W decay mode, but may contain events attributable to different decays. The categories will tend to contain events exclusively collected by a given single trigger data stream, except for the eμ and μe categories that contain a significant overlap between the electron and muon triggers. Overlap between the two data

streams is removed vetoing events in the electron data stream that already appear in the single muon trigger. Because the tau lepton is not detected directly but through its decay products, all categories will contain a mixture of events with final states containing electrons, muons, or jets originating from either the W or intermediate τ decays. This ambiguity in reconstruction is maximal in the $\ell\tau_h$ categories because of the higher probability of misidentifying a jet originating from the W decays as originating from a τ lepton decay.

To further improve sensitivity to specific branching fractions, and to constrain some of the systematic uncertainties, the data are further categorized based on the jet and b tag multiplicities as shown in Table 2. Events in the $e\tau_h$ and $\mu\tau_h$ categories with $N_j \leq 1$ and $N_b = 0$, which are used as control regions for τ_h identification, include additional requirements to enhance the proportion of Drell–Yan events: $40 \leq m_{\ell\tau_h} \leq 100\,\text{GeV}$, $\Delta\phi(\ell, \tau_h) > 2.5$, and $m_T^\ell < 60\,\text{GeV}$ where m_T^ℓ is the transverse mass of the electron or muon, $m_T^\ell = \sqrt{2p_T^\ell E_T^{\text{miss}}(1 - \cos\Delta\phi(p_T^\ell, E_T^{\text{miss}}))}$.

Table 2: Categorization of events with electron, muon, and/or tau leptons passing the reconstruction criteria, based on their jet and b-tagged jet multiplicities.

<table>
<tr><th></th><th>$N_j = 0$</th><th>$N_j = 1$</th><th>$N_j = 2$</th><th>$N_j = 3$</th><th>$N_j \geq 4$</th></tr>
<tr><td>$N_b = 0$</td><td>$e\tau, \mu\tau,$
$e\mu$</td><td>$e\tau, \mu\tau,$
$e\mu$</td><td colspan="3">$e\tau, \mu\tau$
$ee, \mu\mu, e\mu$</td></tr>
<tr><td>$N_b = 1$</td><td></td><td>$e\tau, \mu\tau, e\mu$</td><td>$e\tau, \mu\tau$</td><td colspan="2">$e\tau, \mu\tau$</td></tr>
<tr><td></td><td></td><td></td><td colspan="3">$ee, \mu\mu, e\mu$</td></tr>
<tr><td></td><td></td><td></td><td></td><td></td><td>eh, μh</td></tr>
<tr><td>$N_b \geq 2$</td><td></td><td></td><td>$e\tau, \mu\tau$</td><td colspan="2">$e\tau, \mu\tau$</td></tr>
<tr><td></td><td></td><td></td><td colspan="3">$ee, \mu\mu, e\mu$</td></tr>
<tr><td></td><td></td><td></td><td></td><td></td><td>eh, μh</td></tr>
</table>

In several of the analysis categories, there is a nonnegligible contamination of nonprompt leptons originating from multijet QCD production. This contamination specifically affects channels targeting semileptonic $t\bar{t}$ decays, as well as decays with hadronic tau leptons in the final state. Two different data-driven methods are used for estimating nonprompt lepton contamination directly from data.

The approach used for eh and μh categories estimates the nonprompt background by relying on a QCD-dominated sideband sample selected by inverting the requirement on the lepton isolation. The method works by first selecting control regions consistent with the production of one electron or muon plus one to three jets. Based on these data sets, the ratio of the number of leptons passing the nominal analysis selection criteria to the number failing them, but passing looser isolation criteria, is measured as a function of the p_T and η of the nonprompt lepton. These ratios are then used to weight events with the same selection as the signal region where the leptons are required to pass the loose requirement but fail the tighter one used to select signal events.

For event categories with a hadronic τ, the QCD contribution is estimated from a sideband selected by inverting the requirement that the leptons have opposite-sign electric charge. The sideband samples, after subtraction of simulated background processes, are scaled by a set of transfer factors determined separately in additional control regions. This method relies on the

fact that there are few SM processes that give rise to this particular type of same-sign final state, and the events instead originate primarily from misidentification of a hadronic jet, or nonprompt lepton, as being a prompt lepton. The simulated processes accounted for include $Z \to \tau\tau$, where the τ charge is mismeasured, and W+jets. The method is verified in a low jet multiplicity control region enriched in QCD, W+jets, and $Z \to \tau\tau$ processes. Transfer factors between the same- and opposite-sign regions are derived by splitting this control region based on whether the e or μ pass the nominal isolation requirement.

6 Extraction of branching fractions

The determination of the W branching fractions is carried out using a maximum likelihood estimation (MLE) approach that fits histogram templates, derived from the signal and background estimates, to the data. For the sake of describing the method, it is useful to encode the branching fractions into a vector,

$$\boldsymbol{\beta} = \{\beta_{\mathrm{e}}, \beta_{\mu}, \beta_{\tau}, \beta_{\mathrm{h}}\}\,, \tag{5}$$

where the subscript indicates the decay mode of the W boson (all hadronic decay modes, h, are grouped together). Taking further into account the different leptonic and hadronic τ decay channels, one can write

$$\boldsymbol{\beta'} = \{\beta_{\mathrm{e}}, \beta_{\mu}, \beta_{\tau} b_{\mathrm{e}}\,, \beta_{\tau} b_{\mu}, \beta_{\tau} b_{\mathrm{h}}, \beta_{\mathrm{h}}\}\,. \tag{6}$$

Because final states with two W bosons are of primary interest, it is necessary to consider all possible decay combinations. This can be represented by the outer product of $\boldsymbol{\beta'}$ with itself,

$$\mathbf{B} = \boldsymbol{\beta'} \otimes \boldsymbol{\beta'}\,, \tag{7}$$

that represents a 36-term symmetric matrix with 21 unique terms.

The signal samples mainly consist of events resulting from the decay of two W bosons, which are split into 21 categories based on inspecting generator-level truth information. The efficiencies for these signal samples can be written in a matrix form, with elements corresponding to those in Eq. (7),

$$\mathbf{E} = \begin{bmatrix} \epsilon_{\mathrm{ee}} & \epsilon_{\mathrm{e}\mu} & \epsilon_{\mathrm{e}\tau_{\mathrm{e}}} & \epsilon_{\mathrm{e}\tau_{\mu}} & \epsilon_{\mathrm{e}\tau_{\mathrm{h}}} & \epsilon_{\mathrm{eh}} \\ \epsilon_{\mathrm{e}\mu} & \epsilon_{\mu\mu} & \epsilon_{\mu\tau_{\mathrm{e}}} & \epsilon_{\mu\tau_{\mu}} & \epsilon_{\mu\tau_{\mathrm{h}}} & \epsilon_{\mu\mathrm{h}} \\ \epsilon_{\mathrm{e}\tau_{\mathrm{e}}} & \epsilon_{\mu\tau_{\mathrm{e}}} & \epsilon_{\tau_{\mathrm{e}}\tau_{\mathrm{e}}} & \epsilon_{\tau_{\mathrm{e}}\tau_{\mu}} & \epsilon_{\tau_{\mathrm{e}}\tau_{\mathrm{h}}} & \epsilon_{\tau_{\mathrm{e}}h} \\ \epsilon_{\mathrm{e}\tau_{\mu}} & \epsilon_{\mu\tau_{\mu}} & \epsilon_{\tau_{\mathrm{e}}\tau_{\mu}} & \epsilon_{\tau_{\mu}\tau_{\mu}} & \epsilon_{\tau_{\mu}\tau_{\mathrm{h}}} & \epsilon_{\tau_{\mu}h} \\ \epsilon_{\mathrm{e}\tau_{\mathrm{h}}} & \epsilon_{\mu\tau_{\mathrm{h}}} & \epsilon_{\tau_{\mathrm{e}}\tau_{\mathrm{h}}} & \epsilon_{\tau_{\mu}\tau_{\mathrm{h}}} & \epsilon_{\tau_{\mathrm{h}}\tau_{\mathrm{h}}} & \epsilon_{\tau_{\mathrm{h}}\mathrm{h}} \\ \epsilon_{\mathrm{eh}} & \epsilon_{\mu\mathrm{h}} & \epsilon_{\tau_{\mathrm{e}}h} & \epsilon_{\tau_{\mu}h} & \epsilon_{\tau_{\mathrm{h}}\mathrm{h}} & \epsilon_{hh} \end{bmatrix}\,, \tag{8}$$

where the subscript on the τ indicates its (electron, muon, or hadronic) decay mode. This matrix is constructed for each lepton category, jet, and b tag bin, and it is further parameterized as a function of category-dependent observables such as the subleading p_{T} lepton. Each individual efficiency is given by the ratio,

$$\epsilon = \frac{\sum_i w_i}{N_{\mathrm{gen}}} \tag{9}$$

where w_i is the weight for event i and N_{gen} is the total number of events generated for the process under consideration. Based on this, the estimated number of events for a given final state can be written as

$$N_f = \sum_{i,j,k \in sig.} \sigma_k \mathcal{L} E_{ijk} \mathcal{B}_{ij} + \sum_{k \in bg} N_k\,, \tag{10}$$

where σ_k is the cross section of each process that contributes to the W decay signal with branching fraction $\mathcal{B}_{ij}$, $\mathcal{L}$ is the integrated luminosity, and N_k is the predicted number of events for background process k. For W+jet events, the vector defined in Eq. (6) is used with the corresponding vector of efficiencies for each decay mode.

For each category, events are further binned based on a single kinematic observable in each category. The observable is selected to enhance the discrimination between decay products that come directly from the W boson decay from those with an intermediate tau lepton decay. The variables that are selected for each lepton flavor category are as follows:

- ee: the subleading electron p_{T},
- $\mu\mu$: the subleading muon p_{T},
- eμ: the subleading lepton p_{T},
- eτ and $\mu\tau$: the tau p_{T},
- e+jet and μ+jet: the triggering lepton p_{T}.

The largest benefit of including this kinematic information comes in the ee, eμ, and $\mu\mu$ categories where the leptons decaying intermediately from a τ tend to have lower momenta than those decaying directly from a W boson.

Templates are generated by binning the data of each category into histograms using the Bayesian block algorithm [37]. The binning is calculated independently for each category based on 10^4 simulated $\mathrm{t\bar{t}}$ events. Effectively, this procedure parameterizes the efficiency matrix in Eq. (8) as a function of the extra variables listed above. The predicted yield in each p_{T} bin i and category j is a linear combination of the signal and background templates,

$$f_{ij}(\boldsymbol{\beta}) = \sum_{k \in signal} s_{ijk}(\boldsymbol{\beta}, \boldsymbol{\theta}) + \sum_{l \in bckgd} b_{ijl}(\boldsymbol{\theta})\,. \tag{11}$$

The effects of various sources of systematic uncertainties are accounted for by incorporating nuisance parameters $\boldsymbol{\theta}$ into the model [38], as described in Section 7. Having constructed the model for the data, the negative log likelihood (NLL) can then be obtained and minimized for values of the W boson branching fractions. Including terms for the nuisance parameters, θ, and their prior uncertainty, $\pi(\theta)$, the NLL can be written as

$$L(\boldsymbol{\beta}, \boldsymbol{\theta}) = \sum_{\mathrm{i} \in \mathrm{channel}} \sum_{\mathrm{j} \in \mathrm{bins}} \Big[-y_{ij} \ln f_{ij}(\boldsymbol{\beta}, \boldsymbol{\theta}) + f_{ij}(\boldsymbol{\beta}, \boldsymbol{\theta}) \Big] + \sum_{\theta \in \boldsymbol{\theta}} \pi(\theta)\,, \tag{12}$$

where y_{ij} is the data yield in p_{T} bin i of category j, and f_{ij} are the templates defined in Eq. (11). The nuisance parameters are treated either as affecting the overall normalization of a channel, or affecting some mixture of the shape of the kinematic distribution being fit and its normalization. For the latter case, morphing templates are generated with the nuisance parameters shifted up and down by one standard deviation. The constraints on nuisance parameters are assumed to be Gaussian. To reduce the impact of some of the more consequential nuisance parameters (e.g., the τ reconstruction efficiency), additional control regions enriched in background processes like $\mathrm{Z} \to \tau\tau$ are included in the fit. The branching fractions are estimated by minimizing Eq. (12) with respect to all parameters over all categories simultaneously. The distributions for all considered event categories are shown in Figs. 1, 2, 3, 4, and 5. The blueish histograms indicate the simulated contributions expected from signal processes, whereas the red, orange, and yellow ones correspond to different backgrounds. By adding extra requirements on the number of b-tagged jets, as can be seen by scanning from left to right the panels of each figure, the data distributions are correspondingly more enriched in signal events.

To cross-check the results derived from the MLE approach, a separate count-based analysis was conducted in parallel. This count-based method does not use kinematic information, and exploits only a selection of categories with a high concentration of $\mathrm{t\bar{t}}$ events. For categories that use the same trigger, ratios of the channel yields are constructed that are then analytically solved for the three leptonic branching fractions from a set of quadratic equations. The method has the benefit of canceling systematics uncertainties related to the $\mathrm{t\bar{t}}$ cross section, trigger efficiency, and luminosity, as well as being robust with respect to the lepton energy calibration. However, its precision is significantly limited by the tau identification systematic uncertainty, and ultimately is less sensitive than the default MLE approach. The resulting branching fractions estimates are found consistent in both methods.

7 Systematic uncertainties

Systematic uncertainties are accounted for through nuisance parameters (n.p.'s), denoted with the θ symbol in Eqs. (11) and (12), in the MLE fit. Each individual source of uncertainty is described next.

The uncertainty of the CMS luminosity estimate is estimated to be 2.5% for the 2016 run [39]. This uncertainty affects the overall normalization of all channels in a fully correlated manner. Each event is weighted by a scale factor to account for differences in the pileup spectrum between data and simulation. The uncertainty of the event weights is mainly due to the uncertainty of the inelastic minimum-bias pp cross section at 13 TeV [40], taken as $\sigma_{\mathrm{MB}} = 69.2 \pm 3.18\,\mathrm{mb}$. The effect of this uncertainty is propagated through the analysis by calculating the distribution of pileup in data while varying the value of σ_{MB} up and down by one standard deviation.

The normalizations of the simulated processes with the largest overall contribution to the signal region ($\mathrm{t\bar{t}}$, Drell–Yan, and W+jets) are accounted for by varying the renormalization and factorization scales, and generating the corresponding morphing templates. The nuisance parameters are assigned independently for different jet multiplicities so that they are uncorrelated before fitting. The remaining processes (tW, and non-WW diboson production) are assigned a single n.p. each, with a 10% uncertainty on their overall normalization.

The uncertainty of the data-driven QCD background estimates is included by assigning a channel-dependent ($\mathrm{e}\mu$, $\mathrm{e}\tau$, $\mu\tau$, eh, and μh) nuisance parameter. For the $\ell\tau$ channels, the uncertainty is estimated based on comparing the transfer factors between same-sign and opposite-sign events in a region where the non-τ lepton is either isolated or anti-isolated. For the semileptonic categories, the normalization is allowed to vary freely, and consequently is constrained by the data themselves.

The uncertainties on the efficiency associated with the reconstruction, trigger, identification, and isolation of electrons and muons are accounted for using p_{T}-dependent nuisance parameters that include the statistical uncertainty as well as systematic variations from the tag-and-probe procedure [41] used to calculate the scale factors. The uncertainty for the muon trigger efficiency is accounted for with a single overall normalization nuisance parameter that assumes a 0.1% prior uncertainty. To account for the muon energy scale, the muon p_{T} is varied in each event by one standard deviation ($\pm 0.2\%$) and the effect is propagated to the morphing templates.

The τ identification and isolation efficiency is accounted for by p_{T}-dependent n.p.'s, and a 5% uncertainty [33] is used as a constraint to each bin. The jet $\to \tau$ scale factors and uncertainties

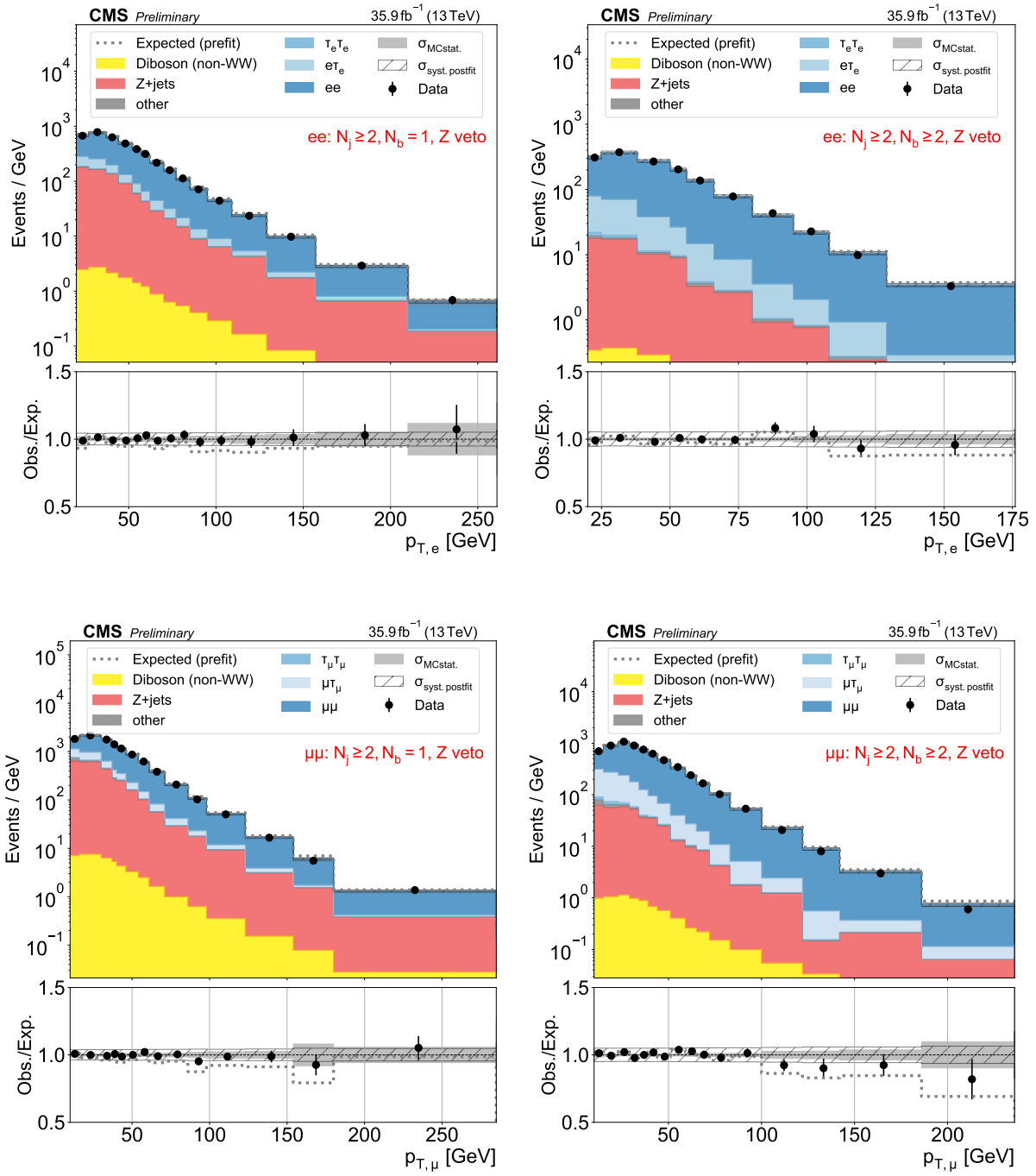

Figure 1: Distributions used as inputs for the binned likelihood fits for the ee (upper) and $\mu\mu$ (lower) categories, with the requirement of one (left) or more than one (right) b-tagged jets. The bottom panels show the ratio of data over prefit (dotted line) and postfit (black circles) expectations, with associated statistical uncertainties (hatched area) and postfit systematic uncertainties (shaded gray).

are derived based on a dilepton plus reconstructed tau control region. A n.p. is assigned to each p_T bin used to determine the scale factor, and an overall normalization n.p. is assigned to account for any difference in rate between light- and heavy-quark jets. The e $\rightarrow \tau$ case where

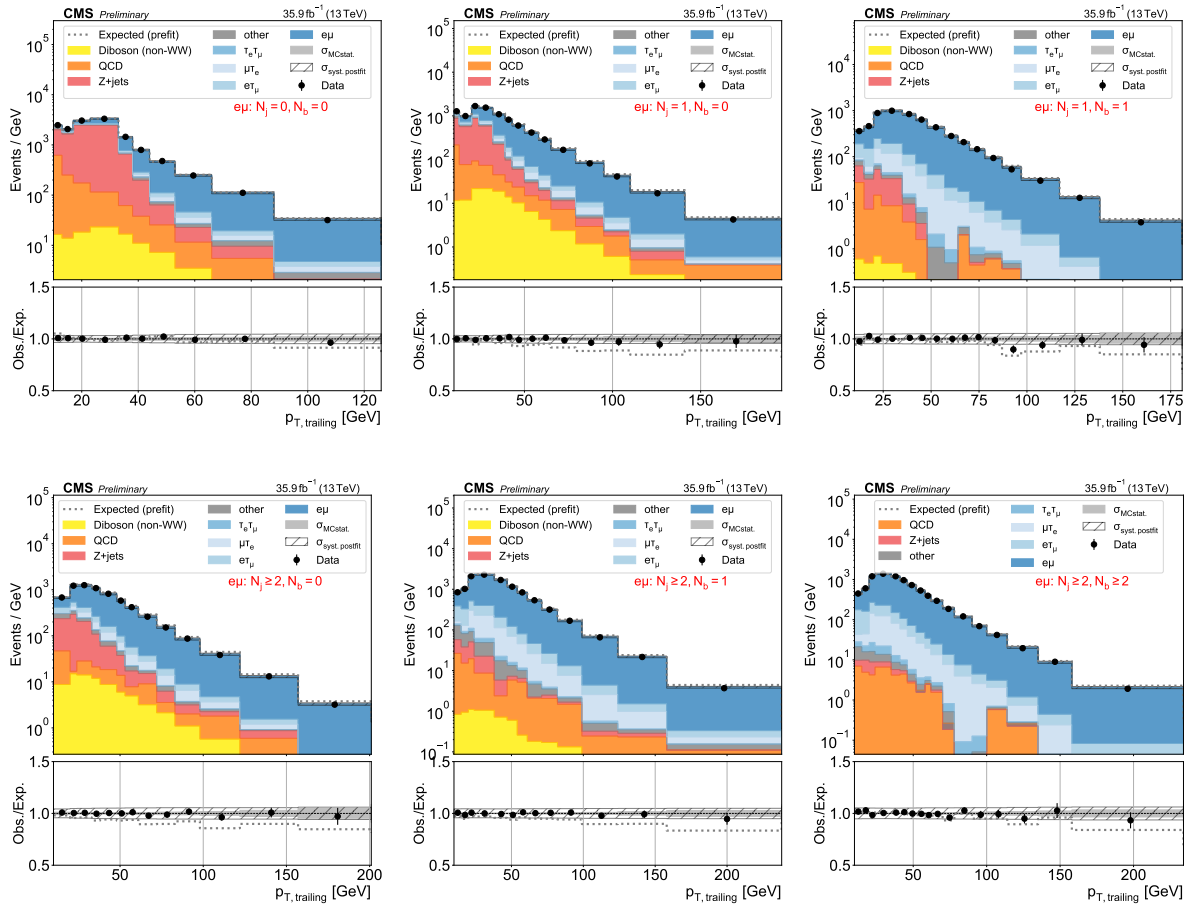

Figure 2: Distributions used as inputs for the binned likelihood fits for the eμ categories. The different panels list the varying selections on the number of jets (N_j) and of b-tagged jets (N_b) required in each case. The bottom panels show the ratio of data over prefit expectations, with the gray histograms (slanted bars) indicating MC statistical (postfit systematic) uncertainties.

an electron is misreconstructed as a hadronically decaying tau is accounted for by a single normalization n.p. The tau energy scale is corrected based on a dedicated independent measurement, and an uncertainty of 1.2% per decay mode is assigned to it. These are included as three different shape uncertainties depending on the reconstructed decay mode of the hadronically decaying tau.

The systematic uncertainties associated to the jet energy scale and resolution impact the analysis by modifying the acceptance of events in the various jet multiplicity categories. Its associated propagated uncertainty is derived by varying the various sources of jet uncertainties, and assessing the resulting effect on the jet and b tag multiplicities. The jet energy scale is varied over various individual uncertainty sources, and incorporated via several shape nuisance parameters. The jet energy is corrected in simulation to account for the difference in resolution between data and simulation. The correction is applied per jet and is dependent on the jet p_T. The overall effect of this procedure is estimated by varying the energy scale factor up and down one standard deviation, and propagating the corresponding effect into the morphing templates.

The b tag modelling in simulation is corrected with scale factors to better describe the data. The uncertainty of the correction is assessed based on up and down variations of b tagging and

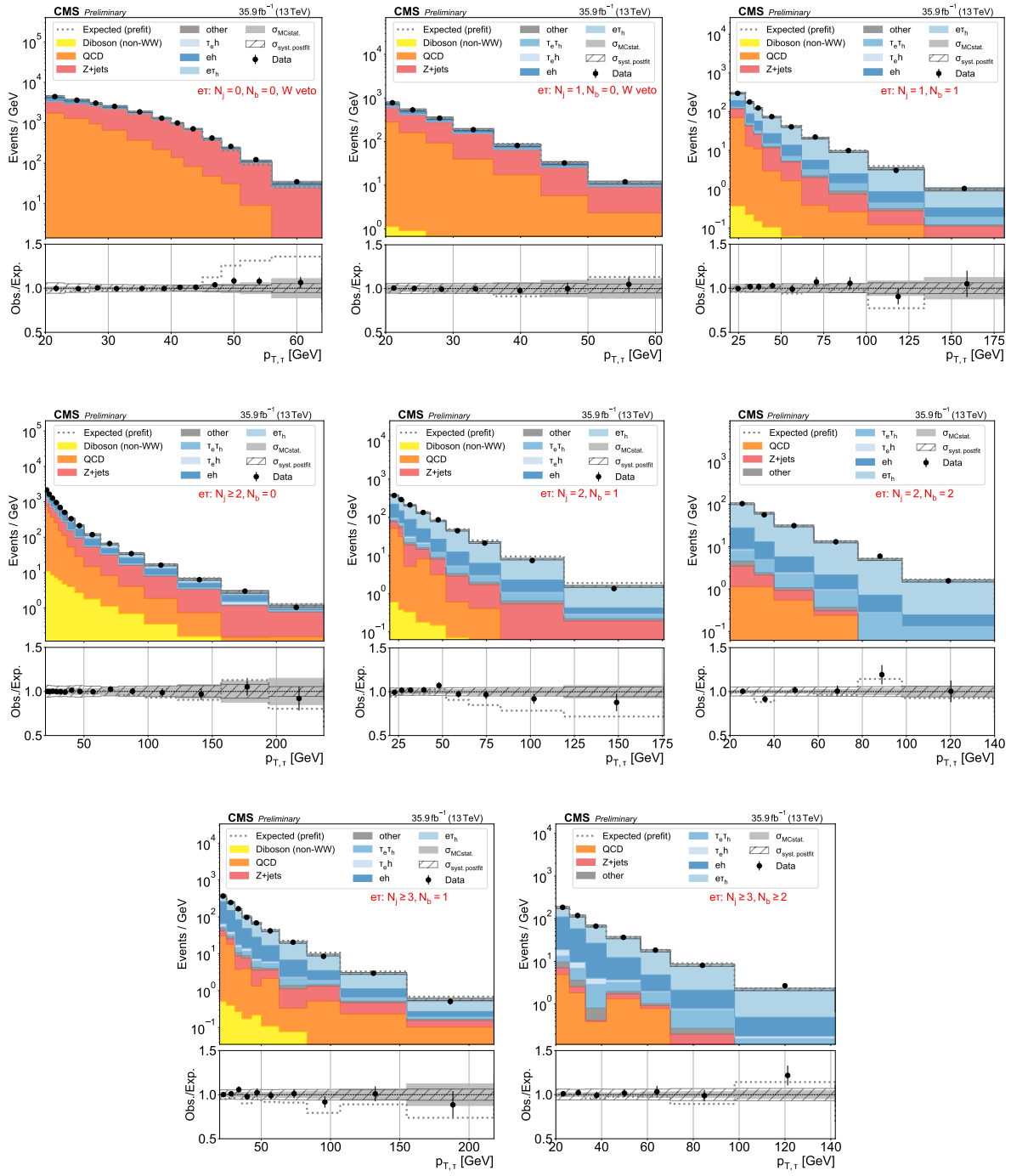

Figure 3: Distributions used as inputs for the binned likelihood fits for the eτ categories. The different panels list the varying selections on the number of jets (N_j) and of b-tagged jets (N_b) required in each case. The bottom panels show the ratio of data over prefit expectations, with the gray band (slanted bars) indicating MC statistical (postfit systematic) uncertainties.

mistagging scale factors determined in the QCD-jet enriched control region. The b tag uncertainties are factorized in the calculation of the scale factors based on their various underlying sources considered. The variation is propagated into the final result through the inclusion of shape n.p.'s for both b tagging and mistagging variations.

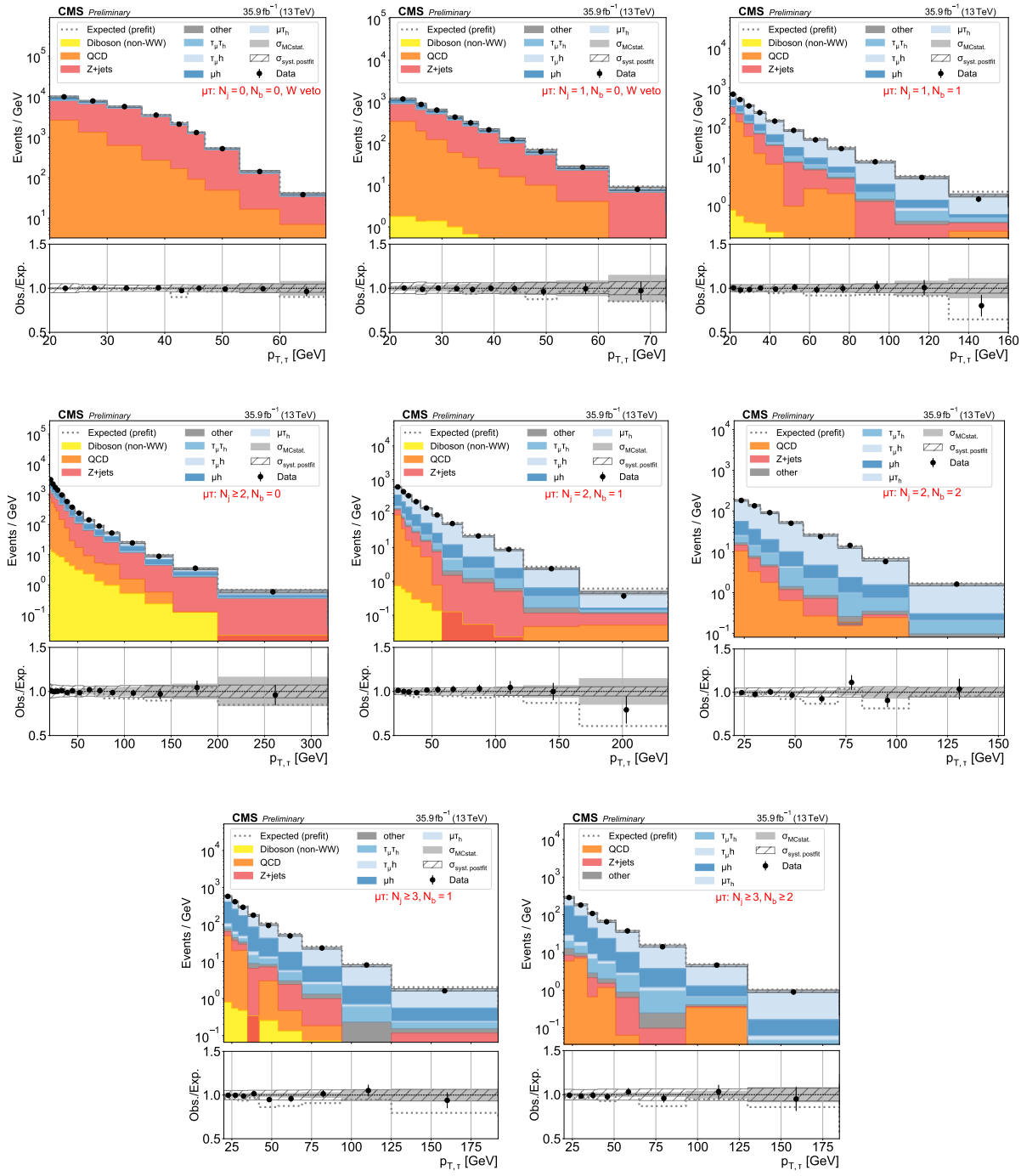

Figure 4: Distributions used as inputs for the binned likelihood fits for the $\mu\tau$ categories. The different panels list the varying selections on the number of jets (N_j) and of b-tagged jets (N_b) required in each case. The bottom panels show the ratio of data over prefit expectations, with the gray histograms (slanted bars) indicating MC statistical (postfit systematic) uncertainties.

The uncertainties associated to the PDFs used in the MC data are accounted for by summing in quadrature the weights of the 100 NNPDF3.0 replicas, and then varying the event weights both up and down by this value. Similarly, each simulated event has weights associated with the nine possible variations of the theoretical renormalization μ_R and factorization μ_F scales. The associated uncertainty of the simulated samples is thereby assessed considering all possible

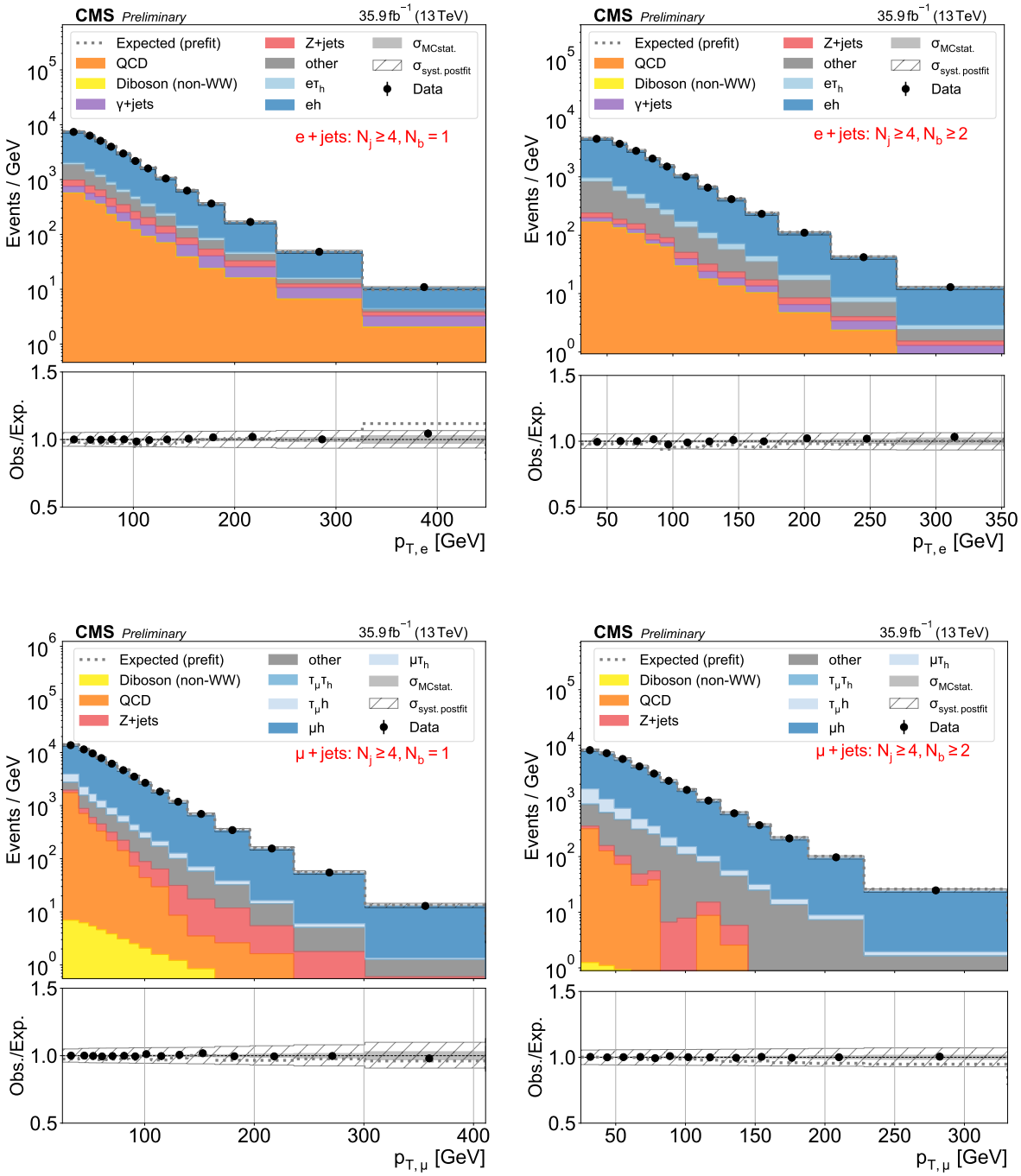

Figure 5: Distributions used as inputs for the binned likelihood fits for the eh (upper) and μh (lower) categories, with the requirement of one (left) or more than one (right) b-tagged jets. The bottom panels show the ratio of data over prefit expectations, with the gray histograms (slanted bars) indicating MC statistical (postfit systematic) uncertainties.

$\mu_{R,F}$ variations, except for the cases where one of the parameters is varied up (down) and the other is varied down (up). This variation is included as a single shape n.p. The impact of variations in the value of α_S, affecting both initial and final state radiation from the colliding partons, is evaluated based on dedicated $t\bar{t}$ MC samples. The matching of the matrix element

calculation to the parton shower is regulated by the *hdamp* parameter at the generator level. This parameter is varied from the nominal value of $1.58^{+0.66}_{-0.59}$ in dedicated MC samples, and propagated into morphing templates. Uncertainties related to the modelling of the underlying event are derived from the PYTHIA CUETP8M2T4 tune variations [42].

The individual impact on the final result from each uncertainty source is estimated by varying the relevant nuisance parameters up and down by their postfit uncertainty, and evaluating the corresponding change in the branching fractions with respect to their central MLE value. The pulls of the nuisance parameters and their impact on the values of the branching fractions are shown in Fig. 6, as relative fractions of the total uncertainty, for each individual W leptonic decay.

8 Results

The values of the branching fractions estimated as described in the previous sections —allowing each branching fraction to vary independently, as well as assuming lepton universality and imposing the three individual branching fractions to be equal, in the MLE fit— are shown in Table 3, and plotted in Fig. 7, compared to the corresponding results determined from a combination of the LEP measurements [3]. The green (yellow) bands in this plot, and in all figures hereafter, indicate the 64% (95%) confidence level (CL) results for the extracted branching fractions. Whereas the systematic uncertainties of the CMS and LEP measurements are similar, the extractions reported here are 3–10 times statistically more precise than those from LEP. The final electron and muon branching fractions are about 1.5 times more precise than measured at LEP, whereas the tau lepton one has a similar uncertainty. Under the assumption of lepton universality, one derives an average leptonic decay branching fraction of $\mathcal{B}(\mathrm{W} \to \ell\overline{\nu}) = (10.89 \pm 0.01 \pm 0.08)\%$ that is consistent with, but much more statistically precise than, the value of $(10.86 \pm 0.06 \pm 0.09)\%$ obtained from the LEP data. The inclusive hadronic W boson decay branching fraction is effectively obtained by imposing $\mathcal{B}(\mathrm{W} \to \mathrm{h}) = 1 - 3\mathcal{B}(\mathrm{W} \to \ell\overline{\nu})$, and has an uncertainty about 15% smaller than that similarly determined at LEP.

The individually extracted branching fractions are strongly correlated because of the composition of the selected data samples, and because of the constraint that the sum of leptonic and hadronic branching fractions is unity. To demonstrate the pairwise correlations between leptonic branching fractions, two-dimensional contours are shown in Fig. 8. For each pair shown in the panels, the third branching fraction that is not plotted has been marginalized over. Additionally, the correlation matrix associated to the branching fractions measurements is shown in Fig. 9. The $\mathcal{B}(\mathrm{W} \to \mathrm{h})$ and $\mathcal{B}(\mathrm{W} \to \tau\overline{\nu}_\tau)$ branching fractions have the largest (anti)correlation (-0.84), whereas $\mathcal{B}(\mathrm{W} \to \mathrm{e}\overline{\nu}_\mathrm{e})$ and $\mathcal{B}(\mathrm{W} \to \tau\overline{\nu}_\tau)$ appear to be the least correlated quantities (0.14 correlation factor).

Having measured the branching fractions, it is of interest to calculate the ratios between them with their associated probability distribution functions (pdfs) in order to compare those to similar results from other experiments where only such ratios have been measured. To transform the likelihood of the branching fractions, $B_\ell = \mathcal{B}(\mathrm{W} \to \ell\overline{\nu})$, to the likelihood of their ratios, $R_{\ell'/\ell}$, the following integral transformation is evaluated [43]

$$f(r) = \int_{-\infty}^{\infty} |\mathcal{B}_\ell| \, g(R_{\ell'/\ell}\mathcal{B}_\ell, \mathcal{B}_\ell) \, dB_\ell \,, \tag{13}$$

where the pdf of the branching fractions $g(\mathcal{B}_{\ell'}, \mathcal{B}_\ell)$ is a bivariate normal distribution with parameters determined from the likelihood fit. It is also possible to carry out the transformation above in the two-dimensional case, so that ratios of tau over muon and electron decays can be

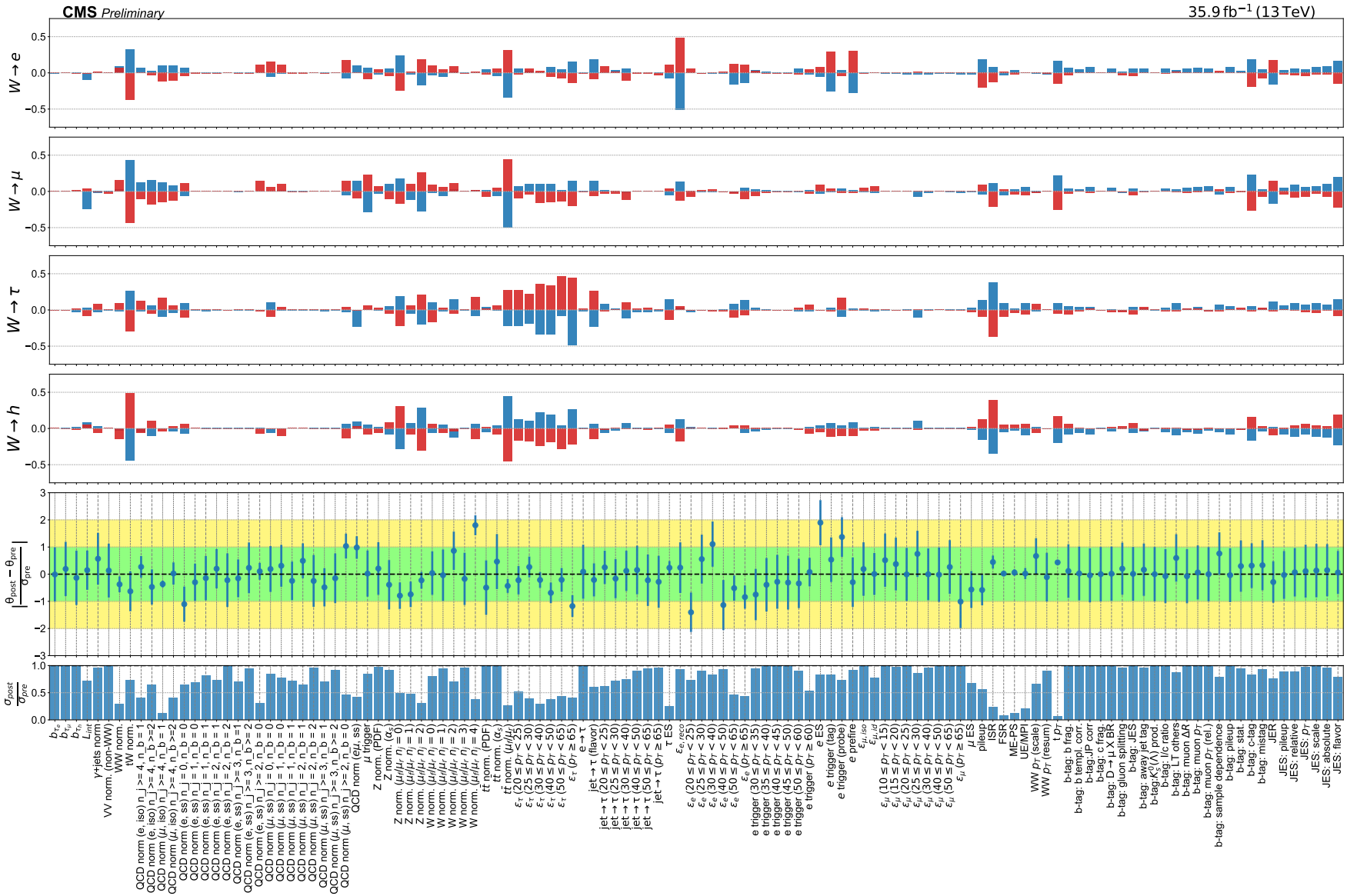

Figure 6: Pulls and impacts of the nuisance parameters on each W leptonic branching fraction. The impacts are calculated with respect to the uncertainty of the corresponding branching fraction component. Error bars on the pull distribution correspond to the postfit uncertainty of the corresponding nuisance parameter.

Table 3: Values of the W branching fractions determined here, compared to the corresponding LEP measurements. The bottom rows list the leptonic W branching fraction derived combining the three individual decay modes assuming lepton universality. Statistical and systematics uncertainties are quoted for each branching fraction.

	CMS	LEP
$\mathcal{B}(W \to e\overline{\nu}_e)$	$(10.83 \pm 0.01 \pm 0.10)\%$	$(10.71 \pm 0.14 \pm 0.07)$ %
$\mathcal{B}(W \to \mu\overline{\nu}_\mu)$	$(10.94 \pm 0.01 \pm 0.08)\%$	$(10.63 \pm 0.13 \pm 0.07)$ %
$\mathcal{B}(W \to \tau\overline{\nu}_\tau)$	$(10.77 \pm 0.05 \pm 0.21)\%$	$(11.38 \pm 0.17 \pm 0.11)$ %
$\mathcal{B}(W \to h)$	$(67.46 \pm 0.04 \pm 0.28)\%$	–
with LU		
$\mathcal{B}(W \to \ell\overline{\nu})$	$(10.89 \pm 0.01 \pm 0.08)\%$	$(10.86 \pm 0.06 \pm 0.09)\%$
$\mathcal{B}(W \to h)$	$(67.32 \pm 0.02 \pm 0.23)\%$	$(67.41 \pm 0.18 \pm 0.20)\%$

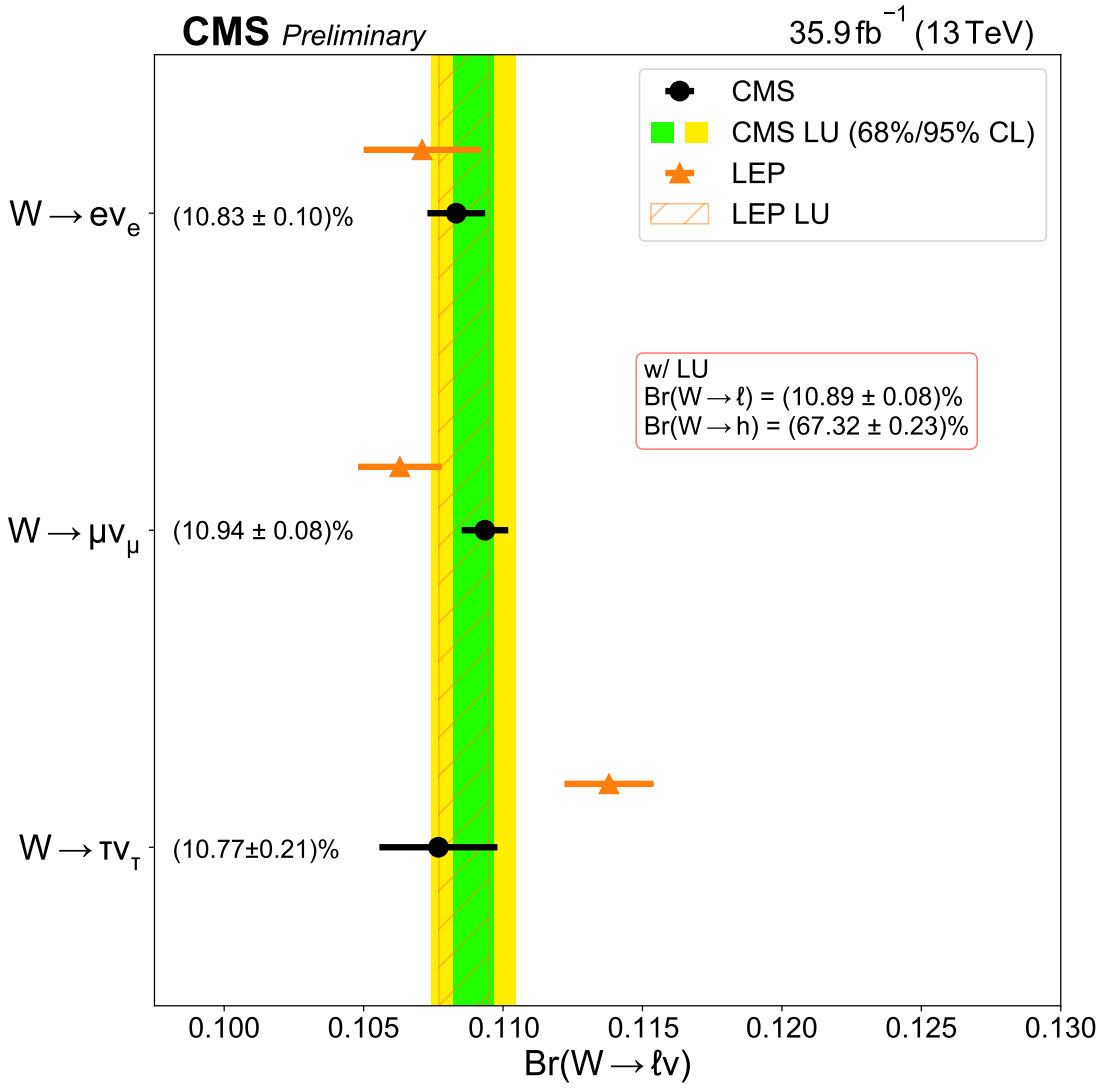

Figure 7: Summary of the measured values of the W leptonic branching fractions compared to the corresponding LEP results [3]. The vertical green-yellow band shows the extracted W leptonic branching fraction assuming lepton universality (the hatched band shows the corresponding LEP result).

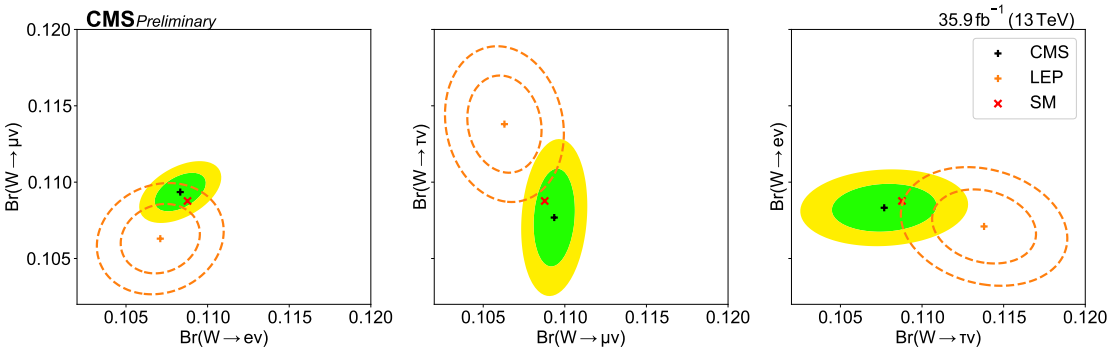

Figure 8: Two-dimensional comparisons of pairs of W leptonic branching fractions derived here, compared to LEP results and to the SM expectation. The green and yellow bands (dashed lines for the LEP results) correspond to the 68% and 95% CL for the resulting two-dimensional Gaussian distribution.

compared between each other as well as to the SM expectation, as shown in Fig. 10. Table 4 lists the ratios constructed from the measurements described above, compared to those measured by LEP and ATLAS.

Table 4: Ratios of different leptonic branching fractions measured in this analysis, and compared to the corresponding LEP and ATLAS results.

	CMS	LEP	ATLAS
$R_{\mu/e} = \mathcal{B}(W \to \mu\overline{\nu}_\mu)/\mathcal{B}(W \to e\overline{\nu}_e)$	1.009 ± 0.009	0.993 ± 0.019	–
$R_{\tau/e} = \mathcal{B}(W \to \tau\overline{\nu}_\tau)/\mathcal{B}(W \to e\overline{\nu}_e)$	0.994 ± 0.021	1.063 ± 0.027	–
$R_{\tau/\mu} = \mathcal{B}(W \to \tau\overline{\nu}_\tau)/\mathcal{B}(W \to \mu\overline{\nu}_\mu)$	0.985 ± 0.020	1.070 ± 0.026	0.992 ± 0.013
$R_{\tau/\ell}$	1.002 ± 0.019	1.066 ± 0.025	–

From the determined values of the inclusive hadronic and leptonic W branching fractions, and following Eq. (2), other interesting SM quantities can be derived such as the QCD coupling at the W mass scale, $\alpha_S(m_W^2)$, or the least well measured of the CKM elements, $|V_{cs}|$, as well as checking the unitarity of the first two rows of the CKM matrix. To extract those SM parameters, one compares the measured ratio of hadronic-to-leptonic branching fractions to the corresponding NLO theoretical expression, leaving either $\alpha_S(m_W^2)$ or the CKM matrix element(s) free,

$$\frac{\mathcal{B}(W \to h)}{1 - \mathcal{B}(W \to h)} = \left(1 + \frac{\alpha_S(m_W^2)}{\pi}\right) \sum_{\substack{i=(u,c),\\ j=(d,s,b)}} |V_{ij}{}^2| = 2.060 \pm 0.021\,, \tag{14}$$

where the value of $\mathcal{B}(W \to h)$ is that extracted when LU is assumed. The theoretical uncertainties of Eq. (14), from parametric dependencies and missing higher-order corrections, are much smaller than the experimental uncertainty for this ratio [6, 10]. If CKM unitarity is imposed, then the sum in Eq. (14) is $\sum |V_{ij}|^2 = 2$ and a value of $\alpha_S(m_W^2) = 0.094 \pm 0.033$ can be derived. This value is clearly not as precise as the current world-average QCD coupling constant, which amounts to $\alpha_S(m_W^2) = 0.1202 \pm 0.0010$ at the W scale [11], but confirms the usefulness of Eq. (14) to extract this fundamental parameter at future ee colliders where the W branching fractions can be measured much more precisely [44]. If, instead, the current world average of $\alpha_S(m_W^2)$ is used in Eq. (14), and the sum in Eq. (14) is left free, a value of $\sum_{ij}|V_{ij}|^2 = 1.989 \pm 0.021$ is obtained that provides a precise test of CKM unitarity. Further solving Eq. (14) for $|V_{cs}|$, and using the more precisely measured values of the other CKM matrix elements in the sum, yields

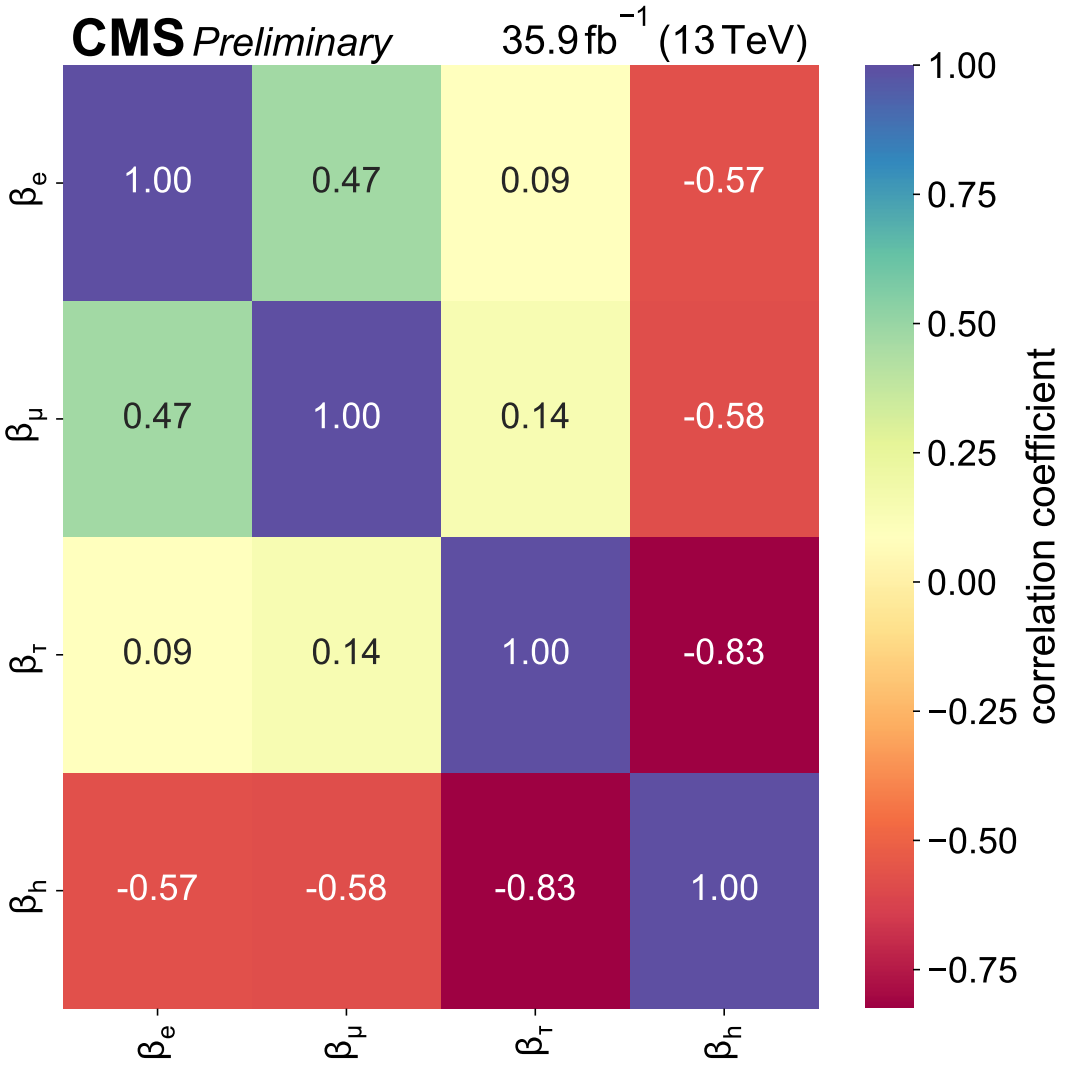

Figure 9: Correlation matrix between the four W boson decay branching fraction components extracted in this work.

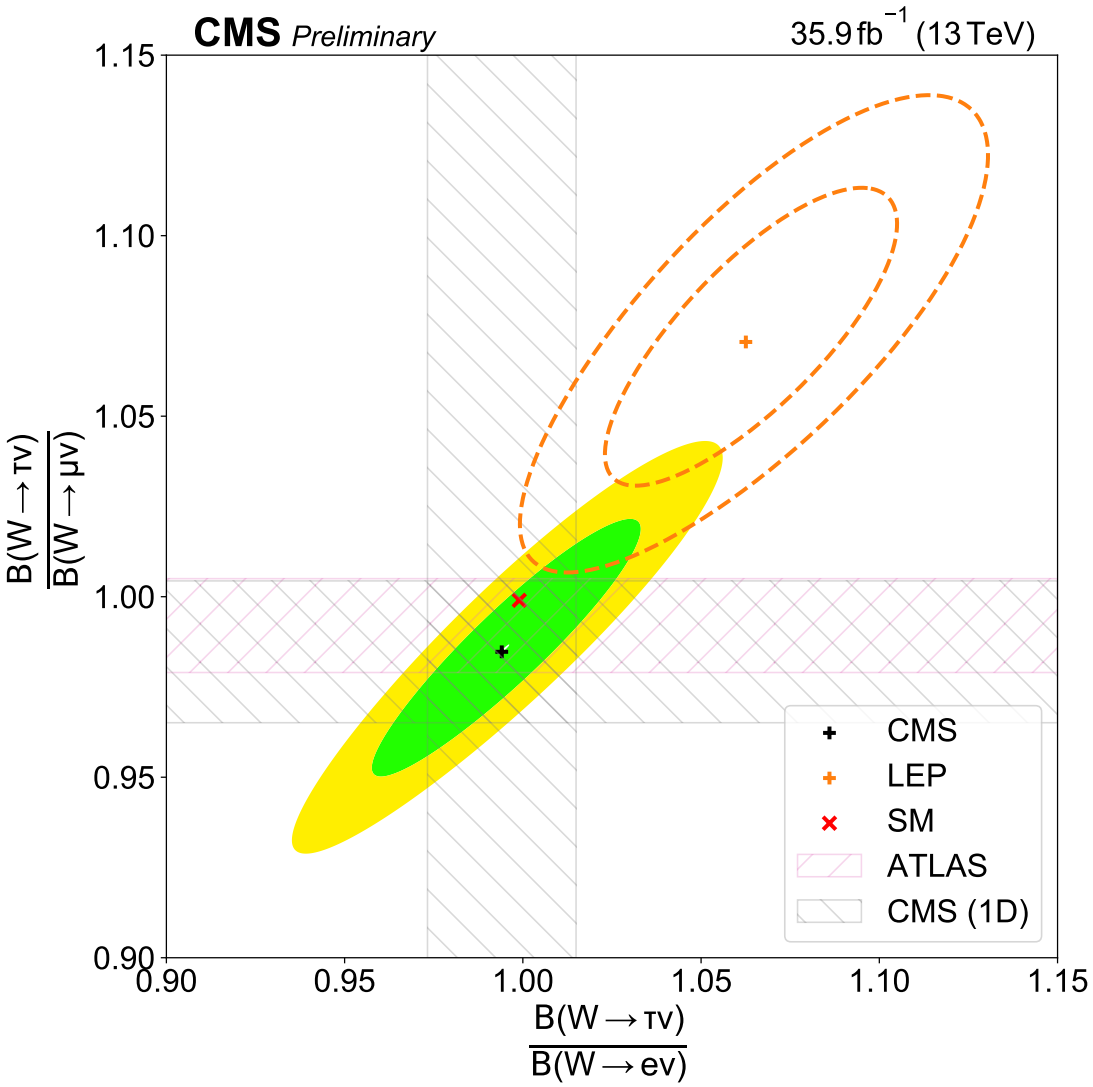

Figure 10: Two-dimensional distributions of the ratios $R_{\tau/e}$ versus $R_{\tau/\mu}$, compared to similar LEP and ATLAS results and to the SM expectation. The green and yellow bands (dashed lines for the LEP results) correspond to the 68% and 95% CL for the resulting two-dimensional Gaussian distribution. The one-dimensional (1D) 68% CL bands are also overlaid for a better visual comparison with the corresponding ATLAS $R_{\tau/\mu}$ result.

a value of $|V_{cs}| = 0.969 \pm 0.011$ that is as precise as the value $|V_{cs}| = 0.987 \pm 0.011$ directly measured from semileptonic D or leptonic D_s decays, using lattice QCD calculations of the semileptonic D form factor or the D_s decay constant [11]. The precision extracting $\alpha_S(m_W^2)$ and $|V_{cs}|$, as well as the CKM unitarity test, are virtually entirely determined by the systematic uncertainty of the inclusive leptonic branching fraction measurement assuming lepton universality.

9 Conclusions

Precise measurements of the three leptonic decay branching fractions of the W boson, as well as of the inclusive leptonic and hadronic ones assuming lepton universality, have been presented. The analysis is based on a data sample of proton-proton collisions at a center-of-mass energy of 13 TeV corresponding to an integrated luminosity of 35.9 fb^{-1} recorded by the CMS experiment during the 2016 run. Events are collected online using single charged lepton triggers that require at least one prompt electron or muon with large transverse momentum. The offline analysis defines categories of final states consistent with the production of two W bosons, or a W boson plus jets, that decay leptonically. The extraction of W boson leptonic branching fractions is carried out through a binned maximum likelihood fit of multiple event categories, where the selected leptonic final states are further classified according to the number of jets as well as of the number of those jets identified as originating from bottom quarks, and binned by channel-dependent kinematic information. The branching fractions for the decay of the W boson into electrons, muons, taus, and hadrons are determined to be $(10.83 \pm 0.10)\%$, $(10.94 \pm 0.08)\%$, $(10.77 \pm 0.21)\%$, and $(67.46 \pm 0.28)\%$, respectively. These results are consistent with the lepton universality hypothesis of the standard model (SM) of particle physics, with a precision that exceeds that achieved by previous measurements based on data collected by the LEP experiments.

When imposing lepton universality while fitting the data, values of $(10.89 \pm 0.08)\%$ and $(67.32 \pm 0.23)\%$ are obtained for the inclusive leptonic and hadronic branching fractions, respectively. From the ratio of inclusive hadronic-to-leptonic branching fractions compared to the corresponding theoretical prediction, further SM quantities can be derived. First, the square sum of the elements of the first two rows of the Cabibbo–Kobayashi–Maskawa (CKM) matrix are found to be $\sum_{ij}|V_{ij}|^2 = 1.989 \pm 0.021$, thereby providing a precise test of CKM unitarity. The $|V_{cs}|$ quark flavor mixing element can be fit similarly, finding $|V_{cs}| = 0.969 \pm 0.011$, which is as precise as the current world-average of $|V_{cs}| = 0.987 \pm 0.011$ obtained from direct D meson decays measurements. Finally, a value of the strong coupling constant at the W mass scale is obtained, $\alpha_S(m_W^2) = 0.094 \pm 0.033$, that, although not competitive compared to the current world average value, confirms the usefulness of the W boson decays to constrain this fundamental SM parameter at future colliders.

References

[1] W. Altmannshofer, P. Stangl, and D. M. Straub, "Interpreting hints for lepton flavor universality violation", *Phys. Rev. D* **96** (2017) 055008, doi:10.1103/PhysRevD.96.055008, arXiv:1704.05435.

[2] LHCb Collaboration, "Search for lepton-universality violation in $B^+ \to K^+\ell^+\ell^-$ decays", *Phys. Rev. Lett.* **122** (2019) 191801, doi:10.1103/PhysRevLett.122.191801, arXiv:1903.09252.

[3] DELPHI, OPAL, LEP Electroweak, ALEPH, L3 Collaboration, "Electroweak measurements in electron-positron collisions at W-boson-pair energies at LEP", *Phys. Rept.* **532** (2013) 119, doi:10.1016/j.physrep.2013.07.004, arXiv:1302.3415.

[4] A. Denner, "Techniques for calculation of electroweak radiative corrections at the one loop level and results for W physics at LEP-200", *Fortsch. Phys.* **41** (1993) 307, doi:10.1002/prop.2190410402, arXiv:0709.1075.

[5] B. A. Kniehl, F. Madricardo, and M. Steinhauser, "Gauge independent W boson partial decay widths", *Phys. Rev. D* **62** (2000) 073010, doi:10.1103/PhysRevD.62.073010, arXiv:hep-ph/0005060.

[6] D. d'Enterria and V. Jacobsen, "Improved strong coupling determinations from hadronic decays of electroweak bosons at N^3LO accuracy", (5, 2020). arXiv:2005.04545.

[7] ATLAS Collaboration, "Test of the universality of τ and μ lepton couplings in W-boson decays from $t\bar{t}$ events with the ATLAS detector", (7, 2020). arXiv:2007.14040.

[8] P. A. Baikov, K. G. Chetyrkin, and J. H. Kuhn, "Order α_s^4 QCD corrections to Z and tau decays", *Phys. Rev. Lett.* **101** (2008) 012002, doi:10.1103/PhysRevLett.101.012002, arXiv:0801.1821.

[9] D. Kara, "Corrections of order $\alpha\alpha_s$ to W boson decays", *Nucl. Phys. B* **877** (2013) 683, doi:10.1016/j.nuclphysb.2013.10.024, arXiv:1307.7190.

[10] D. d'Enterria and M. Srebre, "α_s and V_{cs} determination, and CKM unitarity test, from W decays at NNLO", *Phys. Lett. B* **763** (2016) 465, doi:10.1016/j.physletb.2016.10.012, arXiv:1603.06501.

[11] Particle Data Group, P. A. Zyla et al., "Review of particle physics", *Prog. Theor. Exp. Phys.* **2020** (2020) 083C01, doi:10.1093/ptep/ptaa104.

[12] CMS Collaboration, "The CMS experiment at the CERN LHC", *JINST* **3** (2008) S08004, doi:10.1088/1748-0221/3/08/S08004.

[13] S. Alioli, P. Nason, C. Oleari, and E. Re, "A general framework for implementing NLO calculations in shower Monte Carlo programs: the POWHEG BOX", *JHEP* **06** (2010) 043, doi:10.1007/JHEP06(2010)043, arXiv:1002.2581.

[14] A. Kardos, P. Nason, and C. Oleari, "Three-jet production in POWHEG", *JHEP* **04** (2014) 043, doi:10.1007/JHEP04(2014)043, arXiv:1402.4001.

[15] S. Frixione and B. R. Webber, "Matching NLO QCD computations and parton shower simulations", *JHEP* **06** (2002) 029, doi:10.1088/1126-6708/2002/06/029, arXiv:hep-ph/0204244.

[16] P. Nason, "A new method for combining NLO QCD with shower Monte Carlo algorithm", *JHEP* **11** (2004) 040, doi:10.1088/1126-6708/2004/11/040, arXiv:hep-ph/0409146.

[17] E. Re, "Single-top Wt-channel production matched with parton showers using the POWHEG method", *Eur. Phys. J. C* **71** (2011) 1547, doi:10.1140/epjc/s10052-011-1547-z, arXiv:1009.2450.

[18] J. Alwall et al., "Madgraph 5: going beyond", *Journal of High Energy Physics* **2011** (Jun, 2011) doi:10.1007/jhep06(2011)128.

[19] J. Alwall et al., "The automated computation of tree-level and next-to-leading order differential cross sections, and their matching to parton shower simulations", *JHEP* **07** (2014) 079, doi:10.1007/JHEP07(2014)079, arXiv:1405.0301.

[20] S. Frixione, P. Nason, and C. Oleari, "Matching NLO QCD computations with parton shower simulations: the POWHEG method", *JHEP* **11** (2007) 070, doi:10.1088/1126-6708/2007/11/070, arXiv:0709.2092.

[21] T. Sjostrand et al., "An introduction to PYTHIA 8.2", *Comput. Phys. Commun.* **191** (2015) 159, doi:10.1016/j.cpc.2015.01.024, arXiv:1410.3012.

[22] P. Skands, S. Carrazza, and J. Rojo, "Tuning PYTHIA 8.1: the Monash 2013 tune", *Eur. Phys. J. C* **74** (2014) 3024, doi:10.1140/epjc/s10052-014-3024-y, arXiv:1404.5630.

[23] GEANT4 Collaboration, "GEANT4—a simulation toolkit", *Nucl. Instrum. Meth. A* **506** (2003) 250, doi:10.1016/S0168-9002(03)01368-8.

[24] CMS Collaboration, "The CMS trigger system", *JINST* **12** (2017) P01020, doi:10.1088/1748-0221/12/01/P01020, arXiv:1609.02366.

[25] CMS Collaboration, "Particle-flow reconstruction and global event description with the CMS detector", *JINST* **12** (2017) P10003, doi:10.1088/1748-0221/12/10/P10003, arXiv:1706.04965.

[26] CMS Collaboration, "Description and performance of track and primary-vertex reconstruction with the CMS tracker", *JINST* **9** (2014) P10009, doi:10.1088/1748-0221/9/10/P10009, arXiv:1405.6569.

[27] CMS Collaboration, "Performance of CMS muon reconstruction in pp collision events at $\sqrt{s} = 7$ TeV", *JINST* **7** (2012) P10002, doi:10.1088/1748-0221/7/10/P10002, arXiv:1206.4071.

[28] CMS Collaboration, "Performance of the CMS muon detector and muon reconstruction with proton-proton collisions at $\sqrt{s} = 13$ TeV", *JINST* **13** (2018) P06015, doi:10.1088/1748-0221/13/06/P06015, arXiv:1804.04528.

[29] S. Baffioni et al., "Electron reconstruction in CMS", *Eur. Phys. J. C* **49** (2007) 1099, doi:10.1140/epjc/s10052-006-0175-5.

[30] CMS Collaboration, "Measurements of properties of the Higgs boson decaying into the four-lepton final state in pp collisions at $\sqrt{s} = 13$ TeV", *JHEP* **11** (2017) 047, doi:10.1007/JHEP11(2017)047, arXiv:1706.09936.

[31] CMS Collaboration, "Performance of electron reconstruction and selection with the CMS detector in proton-proton collisions at $\sqrt{s} = 8$ TeV", *JINST* **10** (2015) P06005, doi:10.1088/1748-0221/10/06/P06005, arXiv:1502.02701.

[32] CMS Collaboration, "Electron and photon reconstruction and identification with the CMS experiment at the CERN LHC", arXiv:2012.06888.

[33] CMS Collaboration, "Performance of reconstruction and identification of τ leptons decaying to hadrons and ν_τ in pp collisions at $\sqrt{s} = 13$ TeV", *JINST* **13** (2018) P10005, doi:10.1088/1748-0221/13/10/P10005, arXiv:1809.02816.

[34] M. Cacciari, G. P. Salam, and G. Soyez, "The anti-k_T jet clustering algorithm", *JHEP* **04** (2008) 063, doi:10.1088/1126-6708/2008/04/063, arXiv:0802.1189.

[35] CMS Collaboration, "Determination of jet energy calibration and transverse momentum resolution in CMS", *JINST* **6** (2011) 11002, doi:10.1088/1748-0221/6/11/P11002, arXiv:1107.4277.

[36] CMS Collaboration, "Identification of heavy-flavour jets with the CMS detector in pp collisions at 13 TeV", *JINST* **13** (2018) P05011, doi:10.1088/1748-0221/13/05/P05011, arXiv:1712.07158.

[37] B. Pollack, S. Bhattacharya, and M. Schmitt, "Bayesian blocks in high energy physics: Better binning made easy!", arXiv:1708.00810.

[38] J. S. Conway, "Incorporating nuisance parameters in likelihoods for multisource spectra", in *Proceedings, PHYSTAT 2011 Workshop on Statistical Issues Related to Discovery Claims in Search Experiments and Unfolding, CERN,Geneva, Switzerland 17-20 January 2011*, p. 115. 2011. arXiv:1103.0354. doi:10.5170/CERN-2011-006.115.

[39] CMS Collaboration, "CMS luminosity measurement for the 2016 data-taking period", CMS Physics Analysis Summary CMS-PAS-LUM-17-001, CERN, 2017.

[40] CMS Collaboration, "Measurement of the inelastic proton-proton cross section at $\sqrt{s} = 13$ TeV", *JHEP* **07** (2018) 161, doi:10.1007/JHEP07(2018)161, arXiv:1802.02613.

[41] CMS Collaboration, "Measurements of inclusive W and Z cross sections in pp collisions at $\sqrt{s} = 7$ TeV", *JHEP* **01** (2011) 080, doi:10.1007/JHEP01(2011)080, arXiv:1012.2466.

[42] CMS Collaboration, "Investigations of the impact of the parton shower tuning in PYTHIA 8 in the modelling of $\mathrm{t\bar{t}}$ at $\sqrt{s} = 8$ and 13 TeV", CMS Physics Analysis Summary CMS-PAS-TOP-16-021, CERN, 2016.

[43] D. V. Hinkley, "On the ratio of two correlated normal random variables", *Biometrika* **56** (1969) 635.

[44] FCC Collaboration, "FCC-ee: The Lepton Collider: Future Circular Collider Conceptual Design Report Volume 2", *Eur. Phys. J. ST* **228** (2019) 261, doi:10.1140/epjst/e2019-900045-4.